OPEN ACCESS

GAVIN PUBLISHERS

Biosensors and Bioelectronics Open Access

Najeeb N, et al. Biosens Bioelectron Open Acc: BBOA-140.

DOI: 10.29011/ 2577-2260.100040

Review Article

Simulation Evaluation of a Label-free Silicon-on-Insulator "Lab on a Chip" Optical Biosensor

Najala Najeeb[1,2], Yaping Zhang[1*], Trevor Benson[2]

[1]Department of Electrical and Electronic Engineering, University of Nottingham, China

[2]Department of Electrical and Electronic Engineering, University of Nottingham, UK

[*]**Corresponding author:** Yaping Zhang, Department of Electrical and Electronic Engineering, University of Nottingham, 199 Taikang East Road, Ningbo, 315100, China. Tel: +8657488182420; Email: yaping.zhang@nottingham.edu.cn

Citation: Najeeb N, Zhang Y, Benson T (2018) Simulation Evaluation of a Label-free Silicon-on-Insulator "Lab on a Chip" Optical Biosensor. Biosens Bioelectron Open Acc: BBOA-140. DOI: 10.29011/ 2577-2260.100040

Received Date: 30 June, 2018; **Accepted Date:** 17 July, 2018; **Published Date:** 23 July, 2018

Abstract

This paper presents the design and optimization of a Silicon-on-Insulator (SOI) "Lab on a Chip" immunosensor, based on interferometer technology, capable of the label-free, real time, parallel detection and identification of multiple analytes with extremely high sensitivity. The basic principles for the biosensor device are evanescent wave sensing and interferometry based on Mach-Zehnder Interferometers (MZIs). For a MZI with a sensing length of 1000μm the theoretical sensitivity is 3.1×10^{-7} Refractive Index Units (RIUs). Sensitivity is further increased by incorporating spiral waveguides to increase the length of the interferometer arms within a given wafer footprint. A spiral of four turns gives a sensing arm length of 3145μm, which takes up an area of 0.06mm^2 and gives a theoretical MZI sensitivity of 9.9×10^{-8} RIUs. The sensitivity of detection of the biosensors developed is at least 10-100 times more sensitive than that of current commercial products. Parallel detection is achieved by exciting multiple sensors in parallel using a 1xN Multimode Interferometer (MMI), where N≤12. Y-junction splitters and Directional Couplers (DCs) are evaluated for splitting purposes. A spot-size converter or grating coupler is used to input and output light to and from the optical waveguides.

Keywords: Directional Coupler; Lab-on-a-Chip; Mach-Zehnder Interferometer; Multimode Interferometer; Spot Size Converter

Introduction

Optical biosensors can be defined as sensor devices which make use of optical principles for the transduction of a biochemical interaction into a suitable output signal. A substantial number of measurements can be made based on emission, absorption, fluorescence, refractometry and polarimetry. Based on the measurements taken optical biosensors can be conveniently categorized into three types; Surface Plasmon Resonance (SPR), Evanescent Field (EF) and photonic crystal. This paper presents the design and optimization of evanescent field sensor based on Mach-Zehnder interferometers. To enable parallel detection and identification of multiple analytes in multiple samples, a splitter in the form of a Multimode Interferometer (MMI), Y-junction splitter or Directional Coupler (DC) is used where each output is connected to a sensor. To couple light in and out of the waveguides, a spot size converter or grating coupler is used. (Figure 1) shows the schematic layout of the proposed biosensor which is constructed with an input coupler, a 1×N splitter, spacers, sensors placed within a microfluidic channel, and output couplers.

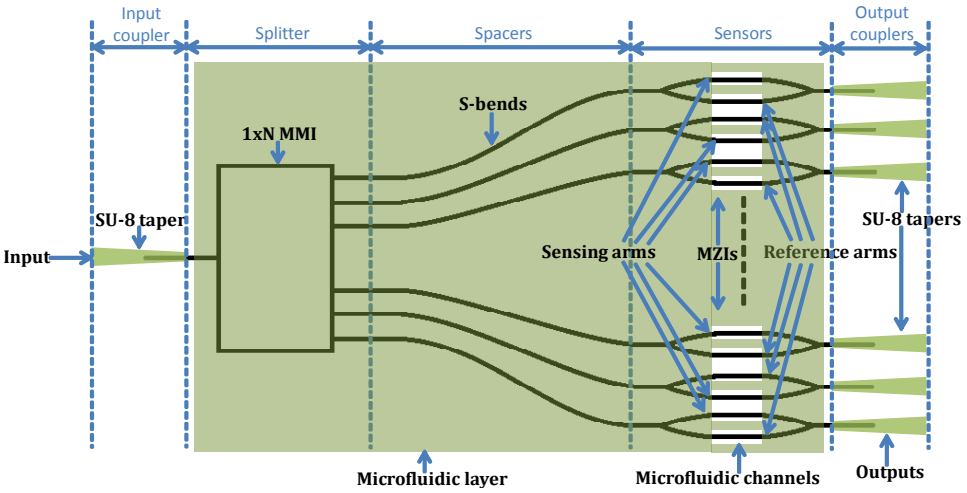

Figure 1: Schematic diagram of the proposed biosensor layout which is made of an input coupler, a 1xN splitter (where N is the number of outputs), separators, sensors, output couplers and a microfluidics layer.

(Figure 2) illustrates the various components of an optical biosensor mentioned in the literature and which are reviewed and optimized in this paper. Each component was simulated and optimized for maximum sensitivity and minimum loss for the fundamental vector TM-like mode. However, the structure with the best simulation result is not always the easiest or cheapest to fabricate. Therefore, considering all advantages and disadvantages each component was carefully selected for the final optical biosensor layout.

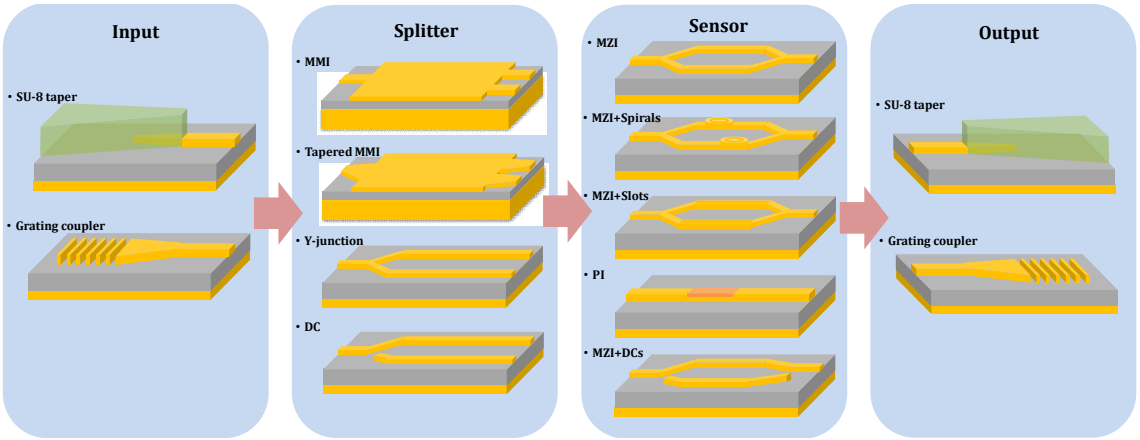

Figure 2: Possible structures considered for the construction of an evanescent wave optical biosensor.

Theory

Light is guided in a high core-cladding refractive index optical waveguide by total internal reflection. During this some of the light travels in the cladding of the waveguide with an amplitude that decays exponentially outwards from the core. The field that penetrates into the upper cladding is the Evanescent Field (EF) that is the basis on which the device operates as a biosensor. This is illustrated schematically in (Figure 3) for the TE polarization. In Figure 3a, the evanescent field is exposed to the upper cladding which can be a solution of refractive index n1 and this type of sensing is referred to as homogenous sensing or bulk sensing. In Figure 3b the evanescent field is exposed to a thin film, also known as an adsorbed layer, attached to the surface of the waveguide with a refractive index n4. This thin film can be composed of antibodies and/or chemical linkers that attach the antibody to the surface of the waveguide. This type of sensing is referred to heterogeneous sensing or surface sensing and is used when the target molecules bind to the antibodies by a chemical reaction. Figure 4 shows the proposed side view of a sensing channel in an evanescent field biosensor.

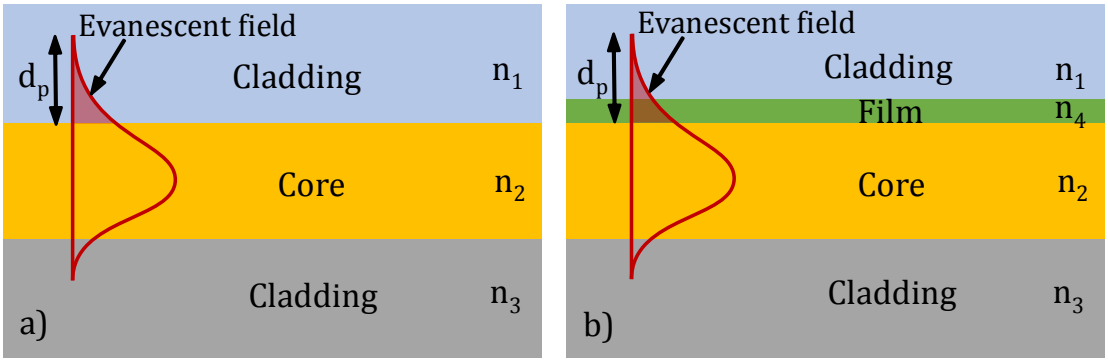

Figures 3(a,b): TE Evanescent Field (EF) in a slab waveguide: **a)** Homogenous or bulk EF sensor and **b)** Surface or adsorbed molecule layer EF sensor.

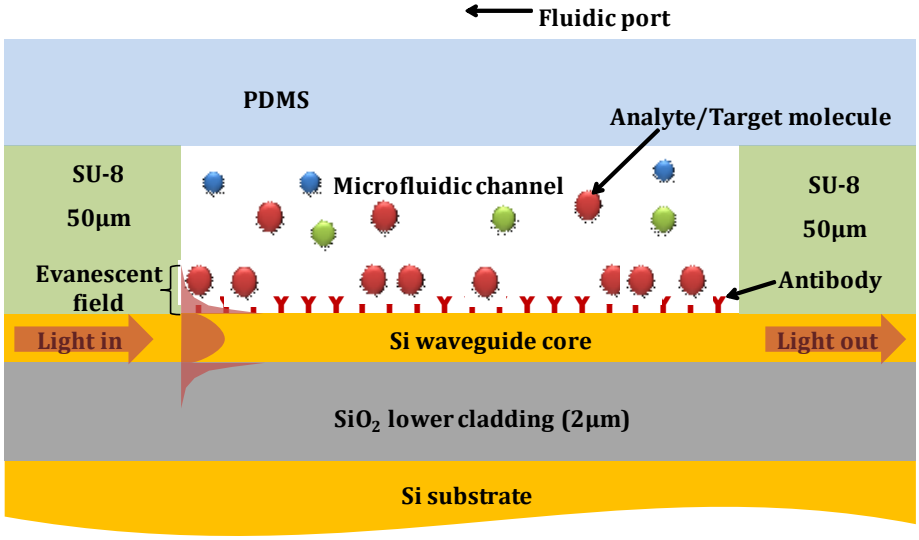

Figure 4: Schematic diagram showing the side view of a sensor window with target molecules that bind with antibodies coated on the waveguide causing a change in refractive index in the evanescent field region of the waveguide.

At the sensing window of the sensor, the waveguide surface is functionalized with antibodies that are specific to the binding of the target molecule. When an analyte is inserted to the cladding at the sensor window, target molecules bind with the receptor molecules changing the refractive index on the surface of the waveguide in the cladding. This results in a change in the effective index of the waveguide (ΔN_{eff}), causing a phase change in the light after propagating for a length L, due to the presence of the evanescent field. Figure 4 also illustrates a microfluidic channel, where simple microfluidic channels and reservoirs were successfully made of SU-8 by photolithography and sealed with Polydimethylsiloxane (PDMS). Silicon based waveguides have been widely researched for biocompatibility and biomedical applications [1,2,3]. Meanwhile SOI material has well established standard fabrication procedures [4,5]. Therefore, SOI material was chosen for the proposed optical biosensor.

Simulation Results

Optimized Core Height of a SOI Waveguide

The first stage of the design was to optimize the SOI waveguide core height to achieve maximum sensitivity. The core height was varied for ridge waveguides of widths 0.5µm and 1µm as illustrated in Figure 5. A width of 0.5µm was used as the waveguide is single mode at the proposed operating wavelength of 1.55µm for this width [6], while a laterally multi-mode ridge width

of 1µm waveguide structure was used for comparison. A 2µm oxide (SiO_2) thickness was used for this project due to wafer availability. The standard industrial oxide thickness is between 1-3µm [5] and in sub-section 3.5 it is shown that an oxide thickness in this range presents low substrate leakage at an operating wavelength around 1.55µm, resulting in an acceptably low propagation loss.

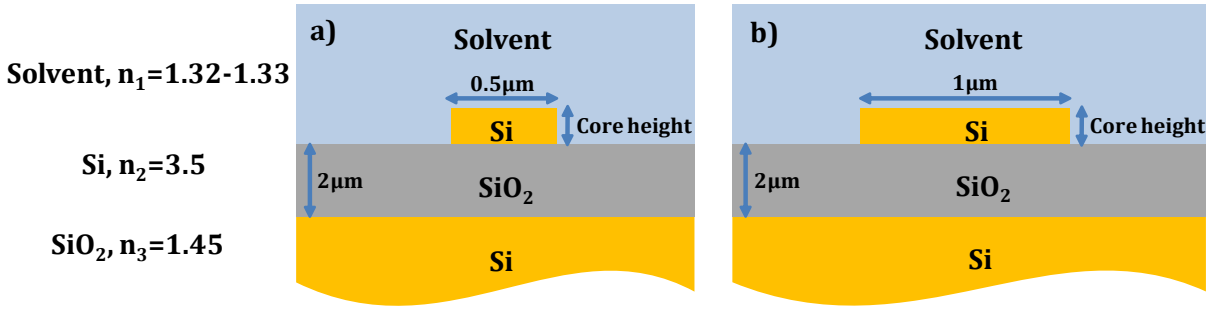

Figure 5(a, b): Ridge waveguide with width **a)** 0.5µm and **b)** 1µm for varying core heights.

The core height was varied from 0.14-0.34µm to ensure the waveguide has vertically single mode operation. The change in cover index, Δn_1, is 1.32-1.33 which assumes the solvent is water based [7]. The sensitivity was calculated using Equation 1 for the vector TE-like and TM-like modes at an operating wavelength of 1.55µm using a commercial software FIMMWAVE. The results are presented in Figure 6.

$$S = \frac{\Delta N_{eff}}{\Delta n_1} \quad (1)$$

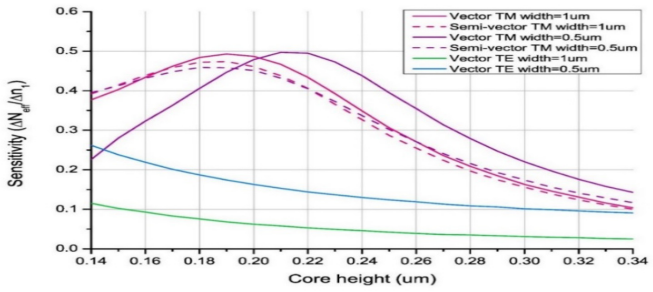

Figure 6: Silicon ridge waveguide sensitivity for vector and semi-vector TE-like and TM-like modes for varying core heights.

From Figure 6, it is shown that the sensitivity obtained for the vector TM-like mode is much higher than that obtained for the vector TE-like mode. The vector TM-like mode sensitivity obtained for waveguide widths of 0.5 µm and 1 µm are similar, while the highest sensitivity is obtained when the core height is in the range of 0.18-0.22 µm. A core height of 0.22µm is preferred in order to take advantage of standard industrial SOI fabrication processes [5].

Optimization of Core Width

In the previous sub-section, the optimum core height was selected to be 0.22 µm. Now the core width was varied within 0.16-0.60µm for the vector TE-like mode and varied within 0.25-0.60 µm for the vector TM-like mode to ensure single mode operation of the waveguide for each polarization. The sensitivity was calculated as described in the previous sub-section and results are presented in Figure 7a. In Figure 7b, when the width of the waveguide is varied the sensitivity of the waveguide changes significantly for the vector TE-like mode whereas the sensitivity is not affected considerably for the vector TM-like mode. Keeping ease, cost and tolerance of fabrication in mind the waveguides in this research will have a fixed core height of 0.22µm and a width of 0.5µm and will operate in the vector TM-like mode with a high waveguide sensitivity of ≈0.5.

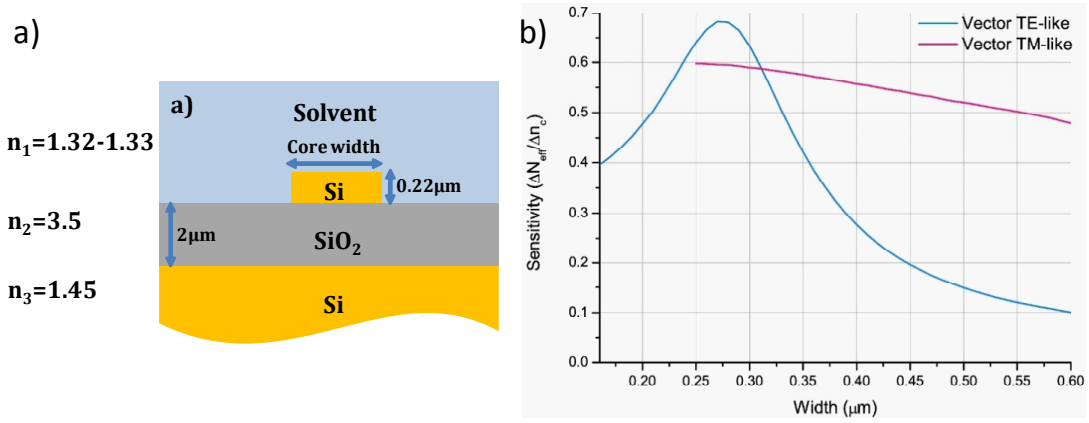

Figures 7(a, b): Ridge waveguide **a)** structure and parameters and **b)** sensitivity for Vector TE-like and Vector TM-like fundamental modes for varying waveguide widths.

Heterogeneous Sensitivity

As explained in section 2, homogeneous sensing occurs when the entire upper cladding (n_1) index changes, causing an effective index change (ΔN_{eff}) in the waveguide. In an immunosensor the waveguides in the sensing window are covered in antibodies which bind to receptor molecules changing the refractive index at the surface of the waveguide. The region that undergoes a change in refractive index is known as the adsorbed layer or adlayer and is illustrated in Figure 8a. The thickness, t of the adsorbed layer was varied from 0 to 1µm and the sensitivity at an operating wavelength of 1.55µm was calculated using Equation 1. The results are illustrated in Figure 8b. From Figure 8b it is shown that the sensitivity has no change when the adsorbed layer thickness is zero. As the thickness increases the sensitivity increases until it reaches its maximum sensitivity of 0.149 and 0.5 for the fundamental vector TE-like and TM-like modes respectively. The thickness of the adsorbed layer at maximum sensitivity is 0.4µm and 0.7µm respectively which means after this point the waveguide would effectively behave like a homogenous sensor.

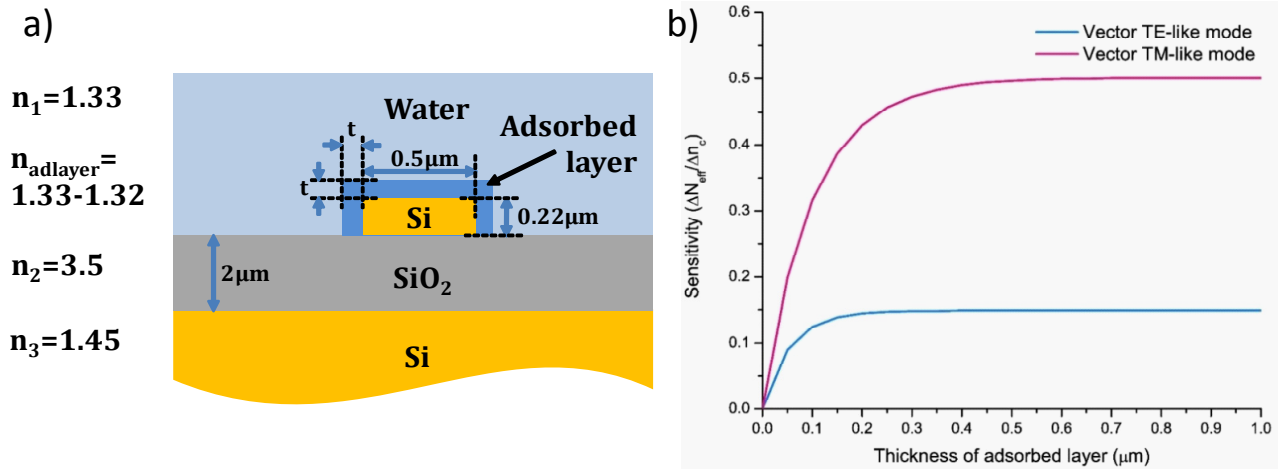

Figures 8(a, b): a) Ridge waveguide with adsorbed layer of thickness, t and **b)** Sensitivity as a function of adsorbed layer thickness for vector TE-like and TM-like modes for a silicon waveguide of height 0.22µm, width 0.5µm and an operating wavelength of 1.55µm.

Slot Waveguides Vs Ridge Waveguides

Slot waveguides, as illustrated schematically in Figure 9, have been mainly used in microring resonators for biosensing applications [8,9]. More recently they have also been explored as planar slot waveguides for fluorescence or absorption based optical sensing [10,11,12]. Dell'Olio and Passaro [11] performed a detailed analysis of this. In this sub-section slot waveguide sensitivity with an edge to edge gap, g, of 100nm is compared to ridge waveguide sensitivity for the vector TE-like and TM-like modes at an operating

wavelength of 1.55 µm. The sensitivity was calculated for varying core widths for a change in cover index, Δn_1, of 1.32-1.33. The results are illustrated in Figure 9.

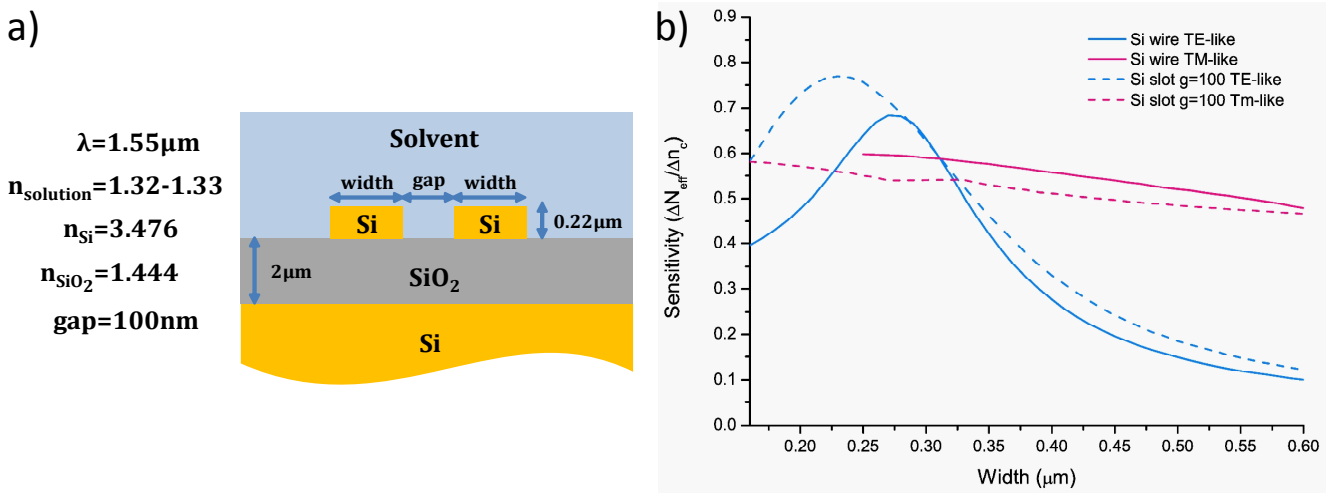

Figure 9: SOI slot waveguide **a)** structure and parameters and **b)** sensitivity as a function of width for quasi-TE and quasi-TM simulated with FIMMWAVE at a wavelength of 1.55µm.

The TM-like mode supported by the Si-wire is more sensitive than the TE-like mode when the width w>0.31µm and the TM-like mode supported by the slot waveguide is more sensitive than the TE-like mode when w>0.33µm. The slot waveguide is more sensitive than the Si-wire for the TE-like mode but less sensitive for the TM-like mode. To achieve the highest sensitivity of 0.77 the device would have to be designed with slot waveguides with g=100nm and w=0.23µm and operate in the TE-like mode. However, the slot waveguides must be integrated into the ridge waveguide system to make use of their high sensitivity in the TE-like mode. The problem of coupling light into a slot waveguide is addressed in the literature [13,14,15,16] by designing efficient strip-slot mode couplers/converters for SOI devices.

The optimum strip and slot waveguide height and width for this research would be 220 × 500 nm and 220 × 230 nm respectively for the fundamental TE-like mode at an operating wavelength of 1.55µm. In theory a strip-slot coupler can be designed with near 100% efficiency which would allow an increase in sensitivity by 48% for the fundamental TE-like mode, but experimentally there would be some loss caused by the strip-slot coupler. Incorporating slot waveguides would not only require an additional strip-to-slot coupler but also polarization sensitive components such as the MMI coupler would have to be redesigned and optimized for the TE-like mode. Long and narrow waveguides slot waveguides would require more sophisticated and expensive fabrication techniques. Therefore, considering mass production and high reproducibility, working with silicon wire waveguides is preferable.

Propagation Loss

As light propagates through the waveguide some loss would be caused even though SOI wires have good confinement. This loss is called the propagation loss and is caused by substrate leakage, scattering at sidewall roughness and material absorption. Pieter Dumon et al. [17], showed the substrate leakage of a SOI Si-wire as a function of buffer thickness (silicon dioxide) for varying core widths for the vector TE-like mode only. In this sub-section, the substrate leakage for an SOI ridge waveguide of core height and width of 0.22 µm and 0.5 µm respectively is calculated for varying SiO_2 buffer thickness for both vector TE-like and TM-like modes at an operating wavelength of 1.55 µm. The results are illustrated in Figure 10. The vector TE-like mode substrate leakage is similar to that presented by Pieter Dumon et al. [17]. It can be observed that the substrate leakage is larger for the vector TM-like mode and for both modes the loss decreases with buffer thickness.

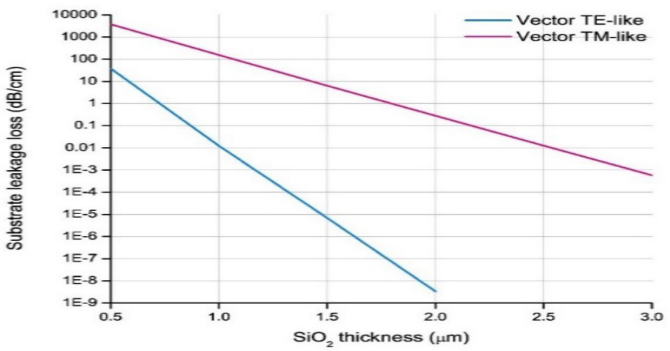

Figure 10: Substrate leakage loss as a function of buffer (SiO_2) thickness for the fundamental vector TE- like and TM-like modes at an operating wavelength of 1.55μm.

Curvature Loss

As shown in the layout of device in Figure 2, the proposed biosensor consists of S-function waveguides, Y-junction splitters, Directional Couplers (DCs), Mach-Zehnder Interferometers with spiral waveguides, all of which require curved or bent waveguides with the smallest possible radius of curvature to achieve a compact device. Light propagating in a bend will be subject to radiation loss [18,19,20] and therefore it is important to determine bending loss as a function of bend radius and hence define the minimum allowable bending radius.

In the literature the minimum bend radius for an SOI waveguide operating at 1.55μm with a fundamental vector TE-like mode was reported to be 2μm, where the loss was 0.15dB for a core of 400×200nm core and 0.6dB for a 300nm square core, while there was no bend related loss when the radius was 5μm or more [15]. Yurii Vlasov et al. [19] showed that when R=5μm, the bend loss is ≈0dB/turn at a wavelength of 1.55μm which is similar to the 0.02dB/cm shown by Zhen Sheng et al. [20] for the vector TE-like mode. Both Vlasov and MacNab [19] and Zhen Sheng et al. [20] did not record the losses for the vector TM-like mode for a wavelength greater than 1450nm as the loss increases exponentially for such narrow radii, as small as 5μm. Figures 11(a, b) show the bending loss of a Si-wire as a function of bend radius for the fundamental vector TE and TM-like modes respectively. Results were obtained from the FIMMWAVE 3D mode solver for the cases when the Si-wire is exposed to air and solution.

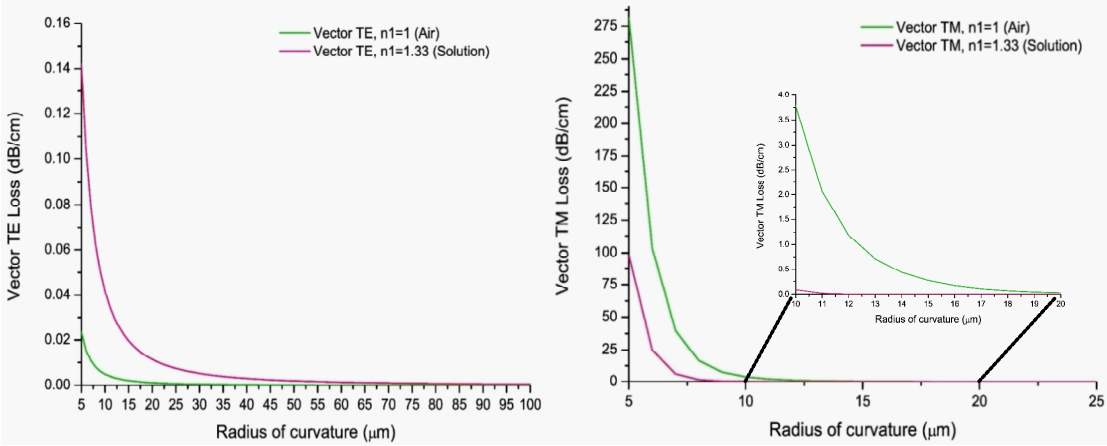

Figures 11(a, b): a) Vector-TE mode and **b)** vector-TM like bending loss as a function of bend radius, R for when a 500×220nm waveguide is exposed to air and solution of refractive index of 1.33 at an operating wavelength of 1.55μm.

From Figure 11(a, b), for the vector TE-like mode the bending loss increases as the index of the cover increases from 1 to 1.33 whereas the opposite is true for the vector TM-like mode. For both vector TE and TM-like modes the bending loss decreases exponentially as the bend radius increases. For the quasi-TE mode and R=5μm, the bending loss is 0.024dB/cm and 0.142dB/cm for n_c=1 and n_c=1.33 respectively which is well below the straight waveguide propagation losses discussed in sub-section 3.5. The curved waveguides in this research will have a cover index of n_c=1.33 or greater and from Figure 11b for bend radius greater than 11μm the loss is negligibly small when n_c=1.33. Therefore, for the vector TM-like mode operation, the minimum bend radius was fixed at 15μm.

Multimode Interference (MMI) Couplers

Multimode Interference (MMI) devices are based on the self-imaging principle where the input image is reproduced into multiple images at the output with high uniformity [21,22]. MMI devices have wide optical bandwidths (in the context of telecommunication systems), low cross talk and are widely used in integrated optics as power splitters [23,24], modulators [25], multiplexers [26], switches [27] and in Mach-Zehnder Interferometers [24]. In

this research, parallel sensing of biological fluid is achieved by connecting Mach Zehnder interferometers to the outputs of an MMI coupler. Figure 12 shows a schematic illustration of a 1x2 MMI coupler.

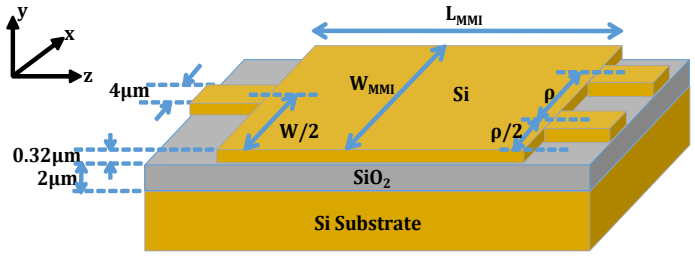

Figure 12: Schematic diagram of a 1x2 MMI structure.

Inside the MMI cavity the beam is split into numerous modes and the symmetric intensity pattern is repeated periodically at the intervals of Λ along the guide. The approximate MMI length, L_{MMI} is calculated by Equation 2 [22]:

$$L_{MMI} = \frac{\Lambda}{N} = \frac{n_{eff} W_{MMI}^{\ 2}}{N \lambda_0} \quad (2)$$

where N is the number of outputs, n_{eff} is the effective refractive index of the MMI cavity, W_{MMI} is the width of the MMI cavity and λ_0 is the operational wavelength. The N images formed are equally spaced across the multimode guide. The transverse distance between the images is known as the 'Pitch', $\rho = W_{MMI}/N$. In this ρ project the is the pitch which is set to 5 µm to avoid cross coupling between the output waveguides. Equation 2 gives only an approximate length as the modes are not strictly confined to the multimode MMI region [28] as is assumed in the derivation of the equation. The exact L_{MMI} is determined by simulating the MMI in FIMMPROP which is a propagation module in FIMMWAVE.

From Figure 1 it is shown that the MMI coupler is covered by the SU-8 polymer microfluidics layer and so for the results in this sub-section the upper cladding index, n1 is set to 1.575 [29]. The input and output waveguides of the MMI coupler have a height and width of 0.22 µm and 0.5 µm respectively. Insertion loss and (output) non-uniformity are the two most commonly used Figures of Merits to compare the efficiency of MMI devices [30,31]. Insertion loss and non-uniformity are defined as Equations 3 and 4:

$$Loss\ insertion\,(dB) = -10 log_{10}\left(\sum_{n=1}^{N} \frac{P_n}{P_{in}}\right) \quad (3)$$

$$Non-uniformity(dB) = -10 log_{10}\left(\frac{P_{min}}{P_{max}}\right) \quad (4)$$

where P_{in} is the input power and P_n is the power of the nth port and P_{min} and P_{max} are the maximum and minimum power observed in the N ports. Insertion loss and non-uniformity calculated for (1×N) MMI couplers up to 1×16 for the vector TM-like mode are presented in Table 1. Table 1 shows a linear increase in L_{MMI} and Insertion Loss as the number of outputs, N, increases. The non-uniformity increases as N increases except for N=8, where it is slightly higher than expected.

N	WMMI (µm)	LMMI (µm)	Insertion Loss (dB)	Non-uniformity (dB)
2	10	68.9	1.35	0
4	20	134.5	1.66	0.01
8	40	268	2.3	1.11
12	60	401.8	2.91	1.01
16	80	537.4	2.97	1.7

Table 1: Insertion loss and non-uniformity for single mode waveguide MMI splitters the vector TM-like mode at a wavelength of 1.55µm.

Tapered MMI Coupler

In the previous sub-section, it was shown that for a 1x2 MMI coupler with input and output waveguide width of 0.5 µm the insertion loss is 1.35 dB. Table 2 shows the insertion loss of the MMI coupler decreases as the input and output waveguide width, w increases. The non-uniformity remains at 0 dB. From Table 2 it can be concluded that a wider w gives a lower insertion loss. However, in sub-section 3.2 the width w was optimized at 0.5 µm for sensing. Therefore, a tapered input and output waveguide is studied as illustrated in Figure 13.

Input/output width (µm)	L_{MMI} (µm)	Insertion loss (dB)	Non-uniformity (dB)
0.5	68.9	1.35	0
1	68.4	1	0
1.5	68	0.21	0
2	69.7	0.08	0

Table 2: Insertion loss and non-uniformity for 1x2 MMI couplers for varying input/output waveguide widths for an operating wavelength of 1.55µm and WMMI of 10µm.

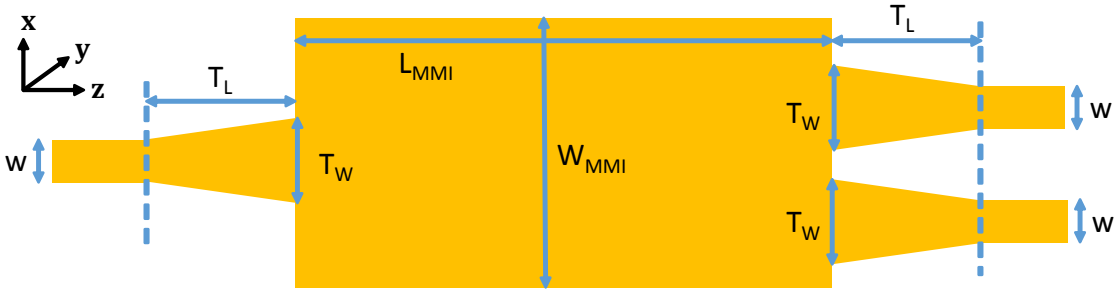

Figure 13: Illustration of a 1x2 MMI with tapered input and output waveguides.

The waveguide width, w and taper width and, Tw are fixed at 0.5 µm and 2µm respectively. The L_{MMI} is optimized for and input/ output waveguide width of 2 µm and a linear taper of optimum length, TL can be designed separately and then combined to save computational time. Thus, a linear taper length, TL, of 50µm is considered where the taper length is long enough to be adiabatic and the insertion loss caused by the taper is assumed negligible. Table 3 shows the insertion loss and non-uniformity for MMI couplers of up to 12 outputs where the MMI input and output waveguide width, TW was fixed at 2 µm. From Table 3 it can be seen that both the insertion loss and non-uniformity increase as N increases, but these values are much lower compared to the corresponding values presented in Table 1 where w was fixed at 0.5µm.

N	W_{MMI} (µm)	L_{MMI} (µm)	Insertion Loss (dB)	Non-uniformity (dB)
2	10	69.7	0.08	0
4	20	136.5	0.19	0.06
8	40	270	0.44	0.44
12	60	405.6	0.57	0.12

Table 3: Insertion loss and non-uniformity for MMI splitters with input/ output waveguide width of 2µm.

S-Function Waveguides

As shown in Figure 1, bent waveguides are used to space the MZI sensors apart and in the construction of the MZI itself. S-function waveguides are also used in the construction of Y-junction splitters and Directional Couplers (DCs). In FIMMWAVE the path of the path of the S-function curve is defined by Equation 5 [32]:

$$P(Z) = P_{lhs}\left(1 - sin^2\left(\frac{\pi Z}{2}\right)\right) + P_{rhs}sin^2\left(\frac{\pi Z}{2}\right) \quad (5)$$

where $Z = (z - z_{in})/L$; zin is the initial z position. Figure 14 illustrates the CAD layout of an S-function waveguide.

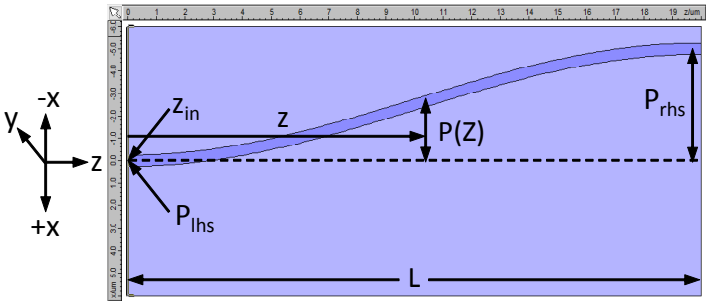

Figure 14: FIMMPROP CAD layout of a S-function waveguide.

As shown in Figure 14 the software lets the user input P_{lhs} and P_{rhs} as the left-hand side and right-hand side offsets from the z axis. Then the user can input the length, L of the waveguide structure. However, from Equation 5 it is not possible to directly calculate the radius of curvature and therefore Equation 6 [33] was used to calculate the radius of curvature at each position along of the curve.

$$R = \frac{\left[1 + \left(\frac{dP}{dz}\right)^2\right]^{\frac{3}{2}}}{\left(\frac{d^2P}{dz^2}\right)} \quad (6)$$

where

$$\frac{dP}{dz} = (P_{rhs} - P_{lhs})\frac{\pi}{2L}\sin\left(\frac{\pi z}{L}\right) \quad (7)$$

$$\frac{d^2P}{dz^2} = (P_{rhs} - P_{lhs})\frac{\pi^2}{2L^2}\cos\left(\frac{\pi z}{L}\right) \quad (8)$$

Equations 6-8 can be used to find the minimum radius of curvature, R_{min} which is expressed by Equation 9:

$$R_{min} = \frac{2L^2}{\pi^2(P_{rhs} - P_{lhs})} \quad (9)$$

This is useful as when P_{lhs}, P_{rhs} and L become larger the simulation window becomes larger making it time consuming, and sometimes impossible, to simulate the transmission loss in the bend using the software. Therefore, using equation 9 the minimum length, L_{min} can be calculated to give $R_{min} = 15\mu m$.

Y-Junction Splitters

Y-junction splitters are described by two S-function waveguides as shown in Figure 15. Y-junction splitters are used in the construction of the MZI and can themselves be used as a 1xN splitter if cascaded. Table 4 shows the insertion loss and non-uniformity of Y-junction splitters when the outputs are spaced 5, 10 and 15 µm apart for the vector TM-like mode at an operating wavelength of 1.55µm for a fixed R_{min} of 15µm. The length and the insertion loss increases as the distance between the outputs, ρ is increased.

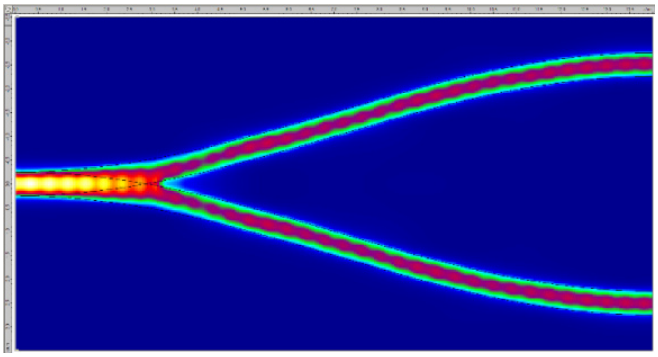

Figure 15: Y-junction splitters.

ρ (µm)	Length (µm)	Insertion loss (dB)	Non-uniformity (dB)
5	14	0.26	0
10	20	0.31	0
20	28	0.44	0

Table 4: Insertion loss and non-uniformity of optimized Y-junction splitters.

Directional Couplers

Directional Couplers (DCs) are constructed from two propagating waveguides set close enough together that energy passing through one is coupled to the other [34]. DCs can be used to replace Y-junctions in the construction of a MZI and cascaded DCs can be used as a 1xN splitter. In this sub-section, DCs are designed and compared with the equivalent Y-junction splitters in terms of insertion loss and length. Figure 16 illustrates a DC where half the light from the propagating lower waveguide is coupled to the non-excited upper waveguide were d is the edge to edge gap between the two waveguides. In order to compare the Y-junction to the DC, S-function waveguides were added to the DC with an output waveguide separation of ρ.

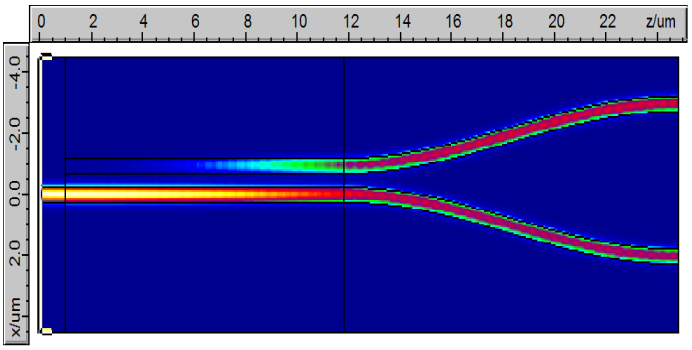

Figure 16: DC coupler designed for the vector TM-like mode where d=0.45µm, coupling length=11.4µm, ρ=5µm, length of S-function waveguides=13µm and the operating wavelength=1.55µm.

DCs are sensitive to wavelength and polarization as the coupling length, L_c for complete power transfer is expressed by Equation 10 [35].

$$L_c = \frac{\pi}{(n_e - n_o)k_o} \qquad (10)$$

where n_e and n_o are the effective refractive indices of the even and odd supermodes supported by the structure and k_o is the free space wavevector. $L_c/2$ is the length required for a 3dB (equal) power splitting as needed for this project? First the optimum coupling length for equal mode intensity was found as d was varied as shown in Figure 17a and the corresponding insertion loss was calculated as shown in Figure 17b. Note that the Y-function waveguides were not included in the results shown in Figure 17.

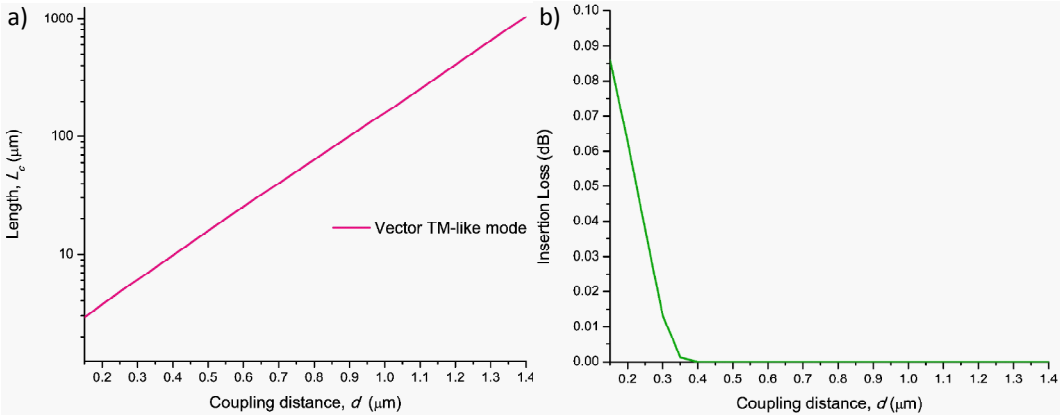

Figures 17(a, b): Vector TM-like mode (Ey) results for DC **a)** coupling length as d is varied and **b)** insertion loss as gap is varied for an operating wavelength of 1.55μm.

From Figure 17a, the length increases logarithmically as the edge to edge coupling distance, d, between the coupling and isolated waveguide is increased. Therefore, to obtain a shorter device a smaller d is preferred. From Figure 17b the insertion loss reduces to ≈0 dB as d ≥ 0.4μm. Therefore, d was fixed to 0.45μm and the coupling length was fixed at 12.46μm for the results shown in Table 5. The results shown in Table 5 include S-function waveguides added to physically separate the outputs of the DC. The length and insertion loss both increase as the final waveguide separation ρ increases.

ρ (μm)	Length (μm)	Insertion loss (dB)	Non-uniformity (dB)
5	24	0.04	0
10	30	0.11	0
20	38	0.3	0

Table 5: Insertion loss and non-uniformity of optimized Y-junction splitters.

Mach-Zehnder Interferometer

Evanescent field sensors based on effective refractive index changes generally operate in interference based systems such as Mach-Zehnder Interferometers (MZIs) [36], Young interferometers [37,38] and ring resonators [39]. These devices use different techniques of superposition to extract phase information about the propagating waves. Figure 18 provides a schematic illustration of a MZI.

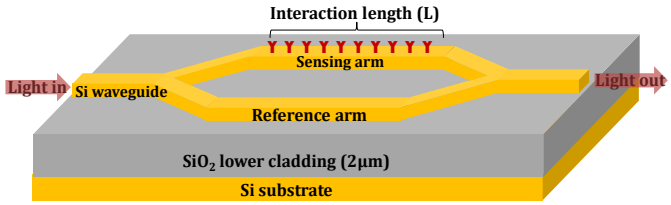

Figure 18: Schematic illustration of a Mach-Zehnder Interferometer (MZI).

The incident light is divided into two equal parts that propagate to the sensing arm and the reference branch respectively. A change in the effective index of the waveguide (ΔN_{eff}) at the sensing window, caused by the binding of the target molecule to the antibody, gives a phase change Δφ in the interaction length, L, as expressed in Equation 11.

$$\Delta\varphi = \Delta N_{eff} \cdot k_0 \cdot L \qquad (11)$$

where k_0 is the free space wave number or the phase constant ($2\pi/\lambda 0$).

The reference branch is used to reduce ambiguity due to external factors such as input power fluctuations, temperature changes in the environment and non-specific adsorption. Non-specific adsorption is when other molecules that are not the target molecule bind with the antibody and cause a phase change. Thus, this reference arm should also be functionalized with the same antibody as the sensing arm, and a similar analyte but without the target molecule should flow over it. When the light from the

sensing and reference arms recombines, constructive or destructive interference occurs; this in turn modulates the light intensity at the single mode output. The output intensity is related to the phase change ($\Delta\varphi$) using Equation 12 [40].

$$I = \frac{1}{2} I_0[1 + \cos(\Delta\varphi)] \qquad (12)$$

where I_0 is the input intensity. The cosinusoidal variation of the interference pattern can be directly related to the concentration of the analyte to be measured via the change in effective refractive index as described in Equation 1. For L=1000µm, $\Delta n_c/2\pi = 0.0031$ rads-1 (assuming $\Delta N_{eff}/\Delta n_c = 0.5$). If a phase resolution of $2\pi \times 10^{-4}$ rads is assumed [40] it gives the device a sensitivity of 3.1×10^{-7} RIUs. In the literature MZIs have been demonstrated with high sensitivity, down to 10^{-6} to 10^{-7} Refractive Index Units (RIUs) [36,40].

MZI with Spirals

As presented in Equation 11 the induced phase change increases as the sensing length increases but in the configuration shown in Figure 18, as the length increases the overall length of the device increases. To counter this problem spiral waveguide are used. Spiral waveguides are increasingly gaining popularity and have recently been used for many applications such as spectrometers [41,42], ring resonators [43,44], filters [43,45], chirpers [46] and Bragg gratings [47]. The most common type of spiral used is the Archimedean spiral which can be expressed in parametric form as Equations 13-14.

$$x = R.cos(\theta) \qquad (13)$$

$$y = R.sin(\theta) \qquad (14)$$

Figure 19 shows a MATLAB plot the two arms of a MZI designed with Archimedean spirals with R_{min}=15µm.

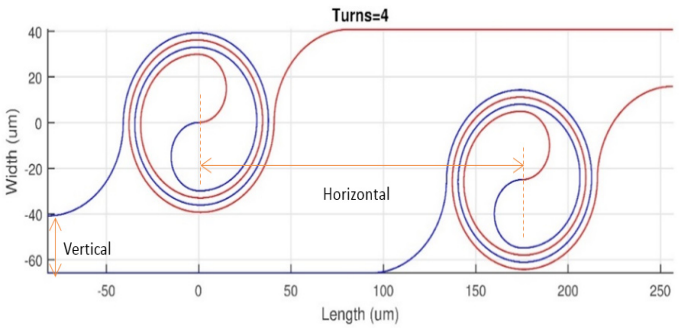

Figure 19: MATLAB layout of the sensing and reference arms of the MZI with spiral waveguides where each spiral has 4 turns.

The two arms are spaced apart, the spacing being described using vertical and horizontal offsets. For the design in Figure 19 the vertical offset was fixed at 25µm so that the Y-junction designed in sub-section 3.10 can be used to connect the two arms to create a MZI. The minimum horizontal offset is set at 4 times the maximum R which in this case is 163µm. Therefore, the horizontal offset was fixed at 175µm. The length of one spiral is given by Equation 15 [48].

$$\text{length of spiral} = \int_{R_{min}}^{R_{max}} \sqrt{\left(\frac{dx}{dR}\right)^2 + \left(\frac{dy}{dR}\right)^2} \qquad (15)$$

Table 6 presents the maximum radius, minimum horizontal offset, horizontal offset used, area of MZI, the length of each arm and sensitivity of spiral MZI for 4, 10, 25 and 40 turns. From Table 6, it can be seen that the footprint or area of the MZI is small compared to the length of each arm achieved thus enabling the device to be as compact as possible while achieving the highest possible sensitivity. However, as the length of the arm increases the device becomes more vulnerable to fabrication errors. The increase in sensitivity (RIU) must be weighed against the complexity and yield of fabrication.

Turns	Maximum Radius (µm)	Minimum horizontal offset (µm)	Horizontal offset used (µm)	Area (Length × width) (µm × µm)	Length of arm (µm)	Sensitivity (RIUs)
4	40.84	163.3	175	0.03mm^2(338.4 × 81.7)	1 175	2.6×10^{-7}
10	59.69	238.7	250	0.06mm^2(488.8 × 119.4)	3 145	9.9×10^{-8}
25	106.81	427.3	450	0.19mm^2(877.2× 213.6)	11 192	2.8×10^{-8}
40	153.94	615.8	625	0.38mm^2(1,239.2 × 307.8)	23 655	1.3×10^{-8}

Table 6: Maximum radius, Minimum horizontal offset, horizontal offset used, area and length of arm of spiral MZI for turns=4, 10, 25 and 40.

Spot-Size Converter

In this sub-section, a spot size converter is designed to propagate a 2±0.5um diameter light beam at a wavelength of 1.55µm into a 0.5 × 0.22µm cross section SOI waveguide with the help of an SU-8 taper as shown in Figure 20. The 2µm thick SU-8 taper sits on an inverted silicon waveguide taper.

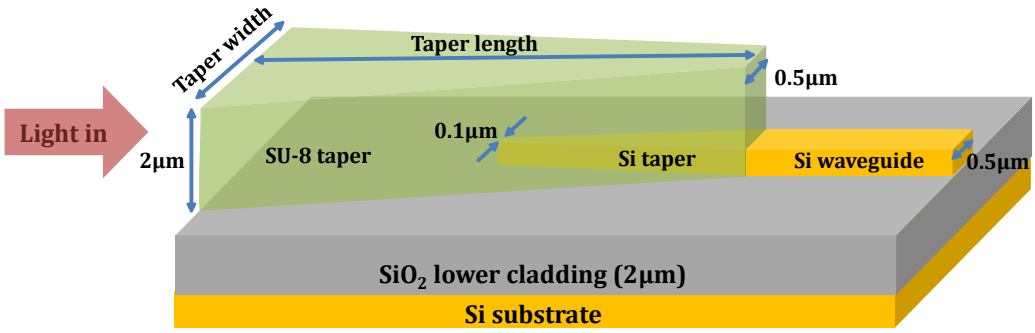

Figure 20: Spot size converter with a tapered SU-8 layer on top of an inverted tapered silicon waveguide.

Pu et al. [49] show that a smaller silicon taper tip width reduces loss; however, it is difficult to fabricate extremely narrow waveguides by etching. Therefore, the silicon taper tip width was limited to 100nm in this project. The length of the SU-8 taper is assumed to be twice the length of the inverted silicon taper for simulation convenience at this point. The width and length of the SU-8 taper were varied as shown in Figures 21(a,b) to obtain maximum transmission. Calculations were performed using FIMMPROP for the vector TM-like mode at an operating wavelength of 1.55µm.

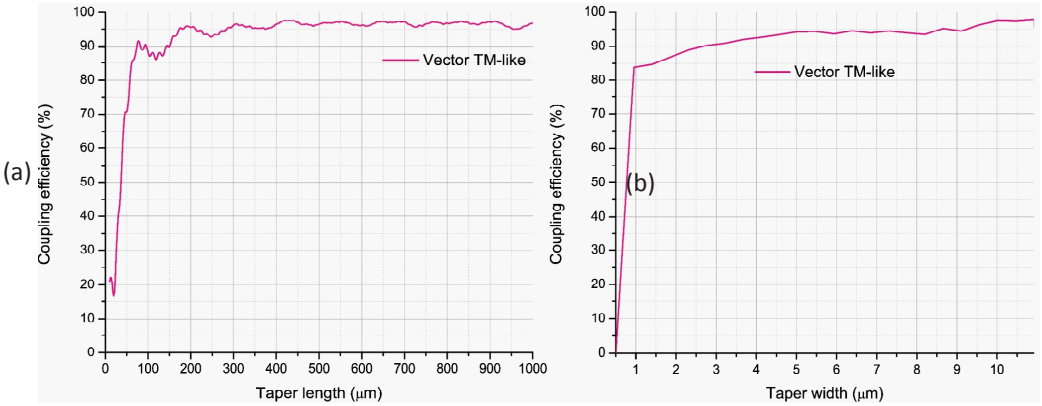

Figures 21(a, b): Spot size converter transmission **(a)** function of SU-8 taper length when taper width=10µm and **(b)** function of SU-8 taper width when taper length=600µm for the vector TM-like mode at an operating wavelength of 1.55µm.

It can be seen from Figures 21(a, b), that in order to obtain a 97.7% transmission the taper length must be at least 400nm and the input taper with width of 10µm. Thus, one might set the taper length to 600µm to allow tolerance when cleaving. In the literature spot size converters have been designed with a rectangular shaped polymer on top of an inverted tapered silicon waveguide, the polymer structure is not tapered. Table 7 compares the results obtained above with the dimensions, insertion loss and experimental coupling efficiency results taken from the literature.

Paper	Silicon taper			Mode	Upper cladding		Insertion Loss (dB)	Coupling efficiency
	Height × width (nm)	Silicon tip (nm)	Length (µm)		material	Height × width (µm)		
[50]	220 × 450	75	150	TE	polymer	2 × 2	1	-

[51]	350 × 300	50	60	TE	SiO_2	1.5 × 5	-	66%
[49]	250 × 480	40	300	TE	SiO_2+Polymer	3.4 ×3.4	0.66	-
				TM			0.36	-
[52]	340 × -	40	200	TE	SU-8	3 × 5	-	60%
				TM			-	60%
This work	220 × 500	100	600	TM	SU-8	2 × tapered from 10 to 0.5	0.1	97.70%

Table 7: Experimental results for spot size converters from literature and theoretical results from this project.

From the literature, the lowest insertion loss for the TM-like mode was measured to be 0.36 dB [49]. By tapering the SU-8 polymer, the insertion loss can be reduced to 0.1dB and the coupling efficiency can be increased to 97.7%.

Grating Couplers

This method is gaining popularity rapidly as aligning the input beam to the waveguide is easier compared to the previous method, even though the input must be at a certain angle as shown in Figure 22. Moreover, the grating coupler is compact.

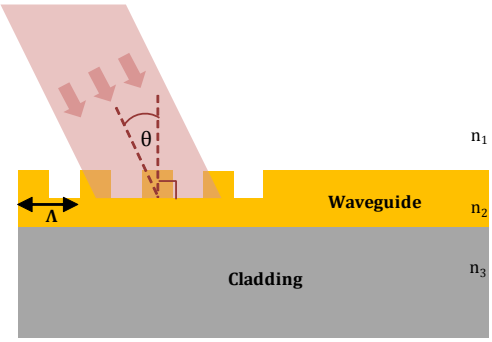

Figure 22: Illustration of grating coupling.

In order to couple light into the waveguide the phase matching condition must be met. This means the propagation constant in the z direction must be the same. This is given by the Equation 16:

$$\beta = k_z = k_0 n_1 \sin\theta \qquad (16)$$

Since $\beta \geq k_0 n_1$, gratings are required to couple light into the waveguide. The period, Λ, of the grating is given by the following Equation 17 [53]:

$$\Lambda = \frac{\lambda_0}{N_{eff} n_1 \sin\theta} \qquad (17)$$

One-Dimensional (1D) grating couplers are polarization sensitive and operate in the vector TE-like mode [54,55]. To operate in the vector TM-like mode, Two-Dimensional (2D) gratings are used [54,56]. Once the grating patterns are optimized the coupling efficiency can be considerably improved further by focusing the gratings, apodization, or focused apodization. Frederik Van Laere et al. [57] designed and fabricated a focused grating coupler for the vector TE-like mode with a theoretical efficiency of 37% for an operating wavelength of 1.55µm. Robert Halir et al. [58] designed an apodized grating coupler and Zhenzhou Chen et al. [59] designed a focused apodized grating coupler where both grating couplers were designed for the vector TM-like mode with a coupling loss of 3.7dB and 3dB respectively. Grating couplers are inefficient compared to spot size converters due to mode mismatch and they require an additional etch step; but they allow for compact and high-density integration of photonic devices which is important for the commercialization of the sensor.

Conclusion

This paper has successfully presented the simulation evaluation of a label-free Silicon-On-Insulator (SOI) optical biosensor. The initial stage of this work was to investigate the ideal material for the transducer and the type of waveguide to obtain a high sensitivity (ΔNeff/Δnc) of detection while also considering biocompatibility, easy integration, and established fabrication procedures for mass production. Calculations showed that High Index Contrast (HIC) materials such as SOI gave the highest sensitivity of 0.47, when the silicon core height was 0.18µm and the upper cladding index, nc was 1.33 for the vector TM-like mode, at an operating wavelength of 1.55µm. SOI based waveguides are also widely used in biomedical applications [1,2,3], allow easy integration and have well established fabrication procedures [4,5].

Simulation investigation performed using the software FIMMWAVE showed that obtaining a high sensitivity of 0.68 is possible if the silicon ridge waveguide height and width was fixed to 0.22µm and 0.27µm respectively and operated in the vector TE-like mode at a wavelength of 1.55µm. The sensitivity can be increased further to 0.77 by using slot waveguides of height and width of 0.22µm and 0.23µm respectively for the vector TE-like mode at a wavelength of 1.55µm. However, the fabrication of such narrow and long waveguides would require sophisticated and expensive fabrication technologies. For wider waveguides, the vector TM-like mode becomes more sensitive than the TE-like

mode. To take advantage of the standard industrial SOI fabrication procedure [5], the silicon ridge waveguide height and width need to be 0.22μm and 0.5μm respectively and operate in the vector TM-like mode at a wavelength of 1.55μm. Due to the availability of SOI wafers two other ridge waveguide dimensions were also used where the silicon ridge waveguide heights were 0.32μm and 0.25μm and the widths were 4μm and 0.8μm respectively.

Propagation loss due to substrate leakage was calculated and showed that as the silicon dioxide thickness separating the silicon guiding layer from the silicon substrate increased, the substrate leakage loss decreased for both the vector TE-like and TM-like modes. The SOI wafers used in this project had a 2μm thick silicon dioxide buffer layer which theoretically gives a substrate leakage loss of 0.23dB/cm for the vector TM-like mode at an operating wavelength of 1.55μm. The curvature loss for the vector TE-like mode increases as the cover index, nc, increases whereas the opposite is true for the vector TM-like mode. For an SOI ridge waveguide of height and width of 0.22μm and 0.5μm respectively and n_c=1.33 operating in the vector TM-like mode at a wavelength of 1.55μm, the calculated curvature loss is 0dB/cm (below calculation error) for a radius of curvature greater than 11μm. Therefore, the minimum radius of curvature was fixed at 15μm for all devices in this project.

Splitting light into two or more waveguides was achieved by Y-junction splitters, Directional Couplers (DCs) and Multimode Interference (MMI) couplers. Simulations show that Y-junction splitters require the shortest device length whereas DCs have the smallest insertion loss. Y-junctions splitters are more vulnerable to fabrication errors due to the sharp splitting of waveguides at the junction. To achieve the splitting of more than two outputs the Y-junction splitters and DCs must be cascaded and with each cascaded section the probability of fabrication errors increases. Therefore, each splitting method has its advantages and disadvantages and all three devices were designed, fabricated and tested successfully. Mach-Zehnder Interferometers (MZIs) constructed by Y-junction splitters, straight waveguides and spiral waveguides were designed, fabricated and tested successfully. The longer the MZI the more sensitive the sensor became. Simulations showed that if the adsorbed layer of a heterogeneous sensor is greater than 0.7μm the sensor acts like a homogeneous sensor. For a homogenous sensing MZI with length, L, of 1000μm and $\Delta N_{eff}/\Delta n_c$ =0.5 the theoretical MZI sensitivity was 3.1×10^{-7} RIUs. For a MZI with spirals of 10 turns and L=3145μm the theoretical MZI sensitivity was 9.9×10^{-8}.

Increasing the sensitivity is not always optimal as the output power intensity is a co-sinusoidal graph which could result in fringe order ambiguity, directional ambiguity and sensitivity fading. This could be avoided by reducing the length of the MZI, thereby reducing the sensitivity, so that the intensity is always located on one arm of the fringe in an intensity graph. Butt coupling and grating coupling methods were used to couple light into and out of waveguides in this project. For butt coupling, a tapered spot size converter was successfully fabricated on top of an inverted silicon taper to efficiently couple the light in and out of the waveguides. Simulations show a 97.7% coupling efficiency and 0.1dB insertion loss for an SU-8 spot size converter tapered from 10μm to 0.5μm with a height of 2μm and a silicon waveguide inversely tapered from 0.1μm to 0.5μm for the vector TM-like mode at an operating wavelength of 1.55μm. The total length of the taper was 600μm.

The grating coupler used was 35μm in length and 24μm in width. The theoretical and experimental coupling efficiency was about 4dB and 7.25dB respectively. Grating couplers require a small area compared to the butt coupling method but have a much higher insertion loss. Label-free SOI optical biosensors based on the evanescent wave principle have been previously demonstrated [36,60]. The novelty of the biosensors in this work lies on the transducer layout, tapered spot size converters and grating couplers, parallel sensing of up to 20 sensors, increased sensitivity and the surface functionalization of the silicon waveguides (not presented in this paper).

References

1. Coffer JL (2014) Semiconducting silicon nanowires for biomedical applications. Elsevier Cambridge.
2. Bañuls MJ, Puchades R, Maquieira Á (2013) Chemical surface modifications for the development of silicon-based label-free Integrated Optical (IO) biosensors: A review Anal Chimica Acta 777: 1-16.
3. Ciampi S, Harper JB, Gooding JJ (2010) Wet chemical routes to the assembly of organic monolayers on silicon surfaces via the formation of Si-C bonds: Surface preparation, passivation and functionalization. Chemical Society Reviews 39: 2158-2183.
4. Kononchuk O, Nguyen BY (2014) Silicon-On-Insulator (SOI) technology: Manufacture and Applications. Elsevier Cambridge.
5. Lim AEJ, Song J, Fang Q, Li C, Tu X, et al. (2014) Review of silicon photonics foundry efforts. IEEE Journal of Selected Topics in Quantum Electronics 20: 405-416.
6. Dumon P, Bogaerts W, Wiaux V, Wouters J, Beckx S, et al. (2004b) Low-loss SOI photonic wires and ring resonators fabricated with deep UV lithography. Photonics Technology Letters IEEE 16: 1328-1330.
7. Segelstein DJ (1981) The complex refractive index of water. M S Thesis, University of Missouri--Kansas City.
8. Claes T, Molera JG, Vos KD, Schacht E, Baets R, et al. (2009) Label-Free Biosensing with a Slot-Waveguide-Based Ring Resonator in Silicon on Insulator. IEEE Photonics Journal 1: 197-204.
9. Baehr-Jones T, Hochberg M, Walker C, Scherer A (2005) High-Q optical resonators in silicon-on-insulator-based slot waveguides. Appl Phys Lett 86: 081101.
10. Bernini R, Cennamo N, Minardo A, Zeni L (2006) Planar Waveguides

for Fluorescence-Based Biosensing: Optimization and Analysis. IEEE Sensors Journal 6: 1218-1226.

11. Dell'Olio F, Passaro VM (2007) Optical sensing by optimized silicon slot waveguides. Optics Express 15: 4977-4993.

12. Barrios, CA (2009) Optical slot-waveguide based biochemical sensors. Sensors 9: 4751-4765.

13. Passaro VMN, La Notte M (2012) Optimizing SOI Slot Waveguide Fabrication Tolerances and Strip-Slot Coupling for Very Efficient Optical Sensing. Sensors (Basel, Switzerland) 12: 2436-2455.

14. Wang Z, Zhu N, Tang Y, Wosinski L, Dai D, et al. (2009) Ultracompact low-loss coupler between strip and slot waveguides. Optics Letters 34: 1498-1500.

15. Palmer R, Alloatti L, Korn D, Heni W, Schindler PC, et al. (2013) Low-Loss Silicon Strip-to-Slot Mode Converters. IEEE Photonics Journal 5: 2200409-2200409.

16. Deng Q, Yan Q, Liu L, Li X, Zhou Z (2015) Highly compact polarization insensitive strip-slot waveguide mode converter. In 2015 Conference on Lasers and Electro-Optics (CLEO): 1-2.

17. Dumon P, Bogaerts W, Wiaux V, Wouters J, Beckx S, et al. (2004a) Low-loss SOI photonic wires and ring resonators fabricated with deep UV lithography. IEEE Photonics Technology Letters 16: 1328-1330.

18. Tsuchizawa T, Yamada K, Fukuda H, Watanabe T, Takahashi Ji, et al. (2005) Microphotonics devices based on silicon microfabrication technology. IEEE Journal of selected topics in quantum electronics 11: 232-240.

19. Vlasov Y, McNab S (2004) Losses in single-mode silicon-on-insulator strip waveguides and bends. Optics Express 12: 1622-1631.

20. Sheng Z, Dai D, He S (2009) Comparative study of losses in ultrasharp silicon-on-insulator nanowire bends. IEEE Journal of Selected Topics in Quantum Electronics 15: 1406-1412.

21. Heaton J, Jenkins R, Wight D, Parker J, Birbeck J, et al (1992) Novel 1□to-N way integrated optical beam splitters using symmetric mode mixing in GaAs/AlGaAs multimode waveguides. Appl Phys Lett 61: 1754-1756.

22. Soldano LB, Pennings ECM (1995) Optical multi-mode interference devices based on self-imaging: principles and applications. Journal of Lightwave Technology13: 615-627.

23. Levy DS, Kyung Hyun P, Scarmozzino R, Osgood RM, Dries C, et al. (1999) Fabrication of ultracompact 3-dB 2 x 2 MMI power splitters. Photonics Technology Letters IEEE 11: 1009-1011.

24. Zhuang L, Wang P, Cao Z, Cao G, Wang Z, et al. (2013) A novel MMI-MZ all-optical switch. Optik - International Journal for Light and Electron Optics 124: 5611-5615.

25. Yue P, Mao BM, Yi X, Li QN, Liu ZJ (2013) A MMI-based ultra-linear high-gain modulator and its performance analysis. Optics & Laser Technology 53: 33-39.

26. Paiam MR, MacDonald RI (1998) A 12-channel phased-array wavelength multiplexer with multimode interference couplers. Photonics Technology Letters IEEE 10: 241-243.

27. Fan W, Jianyi Y, Limei C, Xiaoqing J, Minghua W (2006) Optical switch based on multimode interference coupler. Photonics Technology Letters IEEE 18: 421-423.

28. Cleary A, Garcia-Blanco S, Glidle A, Aitchison JS, Laybourn P, et al. (2005) An integrated fluorescence array as a platform for lab-on-a-chip technology using multimode interference splitters. Sensors Journal IEEE 5: 1315-1320.

29. Sum T, Bettiol A, Van Kan J, Watt F, Pun E, et al. (2003) Proton beam writing of low-loss polymer optical waveguides. Appl Phys Lett 83: 1707-1709.

30. Yin R, Yang J, Jiang X, Li J, Wang M (2000) Improved approach to low-loss and high-uniformity MMI devices. Optics Communications 181: 317-321.

31. Shi Y, Dai D, He S (2005) Improved performance of a silicon-on-insulator-based multimode interference coupler by using taper structures. Optics Communications 253: 276-282.

32. Design P (1997-2012) FIMMPROP Version 5.4.1 Manual.

33. (2017) Arc Length of a Curve.

34. Marcatili EA (1969) Dielectric rectangular waveguide and directional coupler for integrated optics. Bell Labs Technical Journal 48: 2071-2102.

35. Kiyat I, Aydinli A, Dagli N (2005) A compact silicon-on-insulator polarization splitter. IEEE Photonics Technology Letters 17: 100-102.

36. Sepulveda B, Del Rio JS, Moreno M, Blanco F, Mayora K, et al. (2006) Optical biosensor microsystems based on the integration of highly sensitive Mach-Zehnder interferometer devices. Journal of Optics A: Pure and Applied Optics 8: S561.

37. Ymeti A, Kanger JS, Wijn R, Lambeck PV, Greve J (2002) Development of a multichannel integrated interferometer immunosensor. Sensors and Actuators B Chemical 83; 1-7.

38. Ymeti A, Kanger JS, Greve J, Besselink GAJ, Lambeck PV, et al. (2005) Integration of microfluidics with a four-channel integrated optical Young interferometer immunosensor. Biosensors and Bioelectronics 20: 1417-1421.

39. Xu DX, Densmore A, Delâge A, Waldron P, McKinnon R, et al. (2008) Folded cavity SOI microring sensors for high sensitivity and real time measurement of biomolecular binding. Opt Express 16: 15137-15148.

40. Heideman RG, Lambeck PV (1999) Remote opto-chemical sensing with extreme sensitivity: design, fabrication and performance of a pigtailed integrated optical phase-modulated Mach-Zehnder interferometer system. Sensors and Actuators B Chemical 61: 100-127.

41. Velasco AV, Cheben P, Bock PJ, Delâge A, Schmid JH, et al. (2013) High-resolution Fourier-transform spectrometer chip with microphotonic silicon spiral waveguides. Optics letters 38: 706-708.

42. Redding B, Liew SF, Bromberg Y, Sarma R, Cao H (2016) Evanescently coupled multimode spiral spectrometer. Optica 3: 956-962.

43. Xu DX, Delâge A, McKinnon R, Vachon M, Ma R, et al. (2010) Archimedean spiral cavity ring resonators in silicon as ultra-compact optical comb filters. Optics Express 18: 1937-1945.

44. Maleeva N, Fistul M, Karpov A, Zhuravel A, Averkin A, et al. (2014)

Electrodynamics of a ring-shaped spiral resonator. Journal of Applied Physics 115: 064910.

45. Bachman KA, Peltzer JJ, Flammer PD, Furtak TE, Collins RT, et al. (2012) Spiral plasmonic nanoantennas as circular polarization transmission filters. Optics Express 20: 1308-1319.

46. Peccianti M, Ferrera M, Razzari L, Morandotti R, Little BE, et al. (2010) Subpicosecond optical pulse compression via an integrated nonlinear chirper. Optics express 18: 7625-7633.

47. Simard AD, Painchaud Y, LaRochelle S (2013) Integrated Bragg gratings in spiral waveguides. Optics express 21: 8953-8963.

48. Arc length of a curve.

49. Pu M, Liu L, Ou H, Yvind K, Hvam JM (2010) Ultra-low-loss inverted taper coupler for silicon-on-insulator ridge waveguide. Optics Communications 283: 3678-3682.

50. McNab SJ, Moll N, Vlasov YA (2003) Ultra-low loss photonic integrated circuit with membrane-type photonic crystal waveguides. Optics Express 11: 2927-2939.

51. Liu Y, Li Y, Fan Z, Xing B, Yu Y, et al. (2009) Fabrication and optical optimization of spot-size converters with strong cladding layers. Journal of Optics a Pure and Applied Optics 11: 085002.

52. Wahlbrink T, Tsai WS, Waldow M, Först M, Bolten J, et al. (2009) Fabrication of high efficiency SOI taper structures. Microelectronic Engineering 86: 1117-1119.

53. Reed GT, Knights AP (2004) Silicon photonics: An introduction. John Wiley & Sons, West Sussex, UK.

54. Andreani LC, Gerace D, Passoni M, Bozzola A, Carroll L (2016) Optimizing grating couplers for silicon photonics. In Transparent Optical Networks (ICTON) 18th International Conference 1-4, IEEE.

55. Roelkens G, Van Thourhout D, Baets R (2007) SOI grating structure for perfectly vertical fiber coupling. In Proceedings of the European Conference on Integrated Optics (ECIO 2007): 4.

56. Tsuchizawa T, Yamada K, Fukuda H, Watanabe T, Takahashi Ji, et al. (2005) Microphotonics devices based on silicon microfabrication technology. IEEE Journal of selected topics in quantum electronics 11: 232-240.

57. Van Laere F, Claes T, Schrauwen J, Scheerlinck S, Bogaerts W, et al. (2007) Compact focusing grating couplers for silicon-on-insulator integrated circuits. IEEE Photonics Technology Letters 19: 1919-1921.

58. Halir R, Cheben P, Schmid J, Ma R, Bedard D, et al. (2010) Continuously apodized fiber-to-chip surface grating coupler with refractive index engineered subwavelength structure. Optics Letters 35: 3243-3245.

59. Cheng Z, Chen X, Wong CY, Xu K, Tsang HK (2012) Apodized focusing subwavelength grating couplers for suspended membrane waveguides. Appl Phys Lett 101: 101104.

60. Densmore A, Xu DX, Waldron P, Janz S, Cheben P, et al. (2006) A silicon-on-insulator photonic wire based evanescent field sensor. Photonics Technology Letters IEEE 18: 2520-2522.